Publications

11-10-2005

Faint Blue Objects in the Hubble Deep Field–South Revealed: White Dwarfs, Subdwarfs, and Quasars

Mukremin Kilic
University of Texas at Austin

Ted von Hippel
University of Texas at Austin, vonhippt@erau.edu

et al.

FAINT BLUE OBJECTS IN THE HUBBLE DEEP FIELD–SOUTH REVEALED: WHITE DWARFS, SUBDWARFS, AND QUASARS[1]

MUKREMIN KILIC,[2] R. A. MENDEZ,[3] TED VON HIPPEL,[2] AND D. E. WINGET[2]

ABSTRACT

We explore the nature of the faint blue objects in the Hubble Deep Field–South. We have derived proper motions for the point sources in the Hubble Deep Field–South using a 3 yr baseline. Combining our proper-motion measurements with spectral energy distribution fitting enabled us to identify four quasars and 42 stars, including three white dwarf candidates. Two of these white dwarf candidates, HDF-S 1444 and 895, are found to display significant proper motion, 21.1 ± 7.9 and 34.9 ± 8.0 mas yr^{-1}, and are consistent with being thick-disk or halo white dwarfs located at $\sim$2 kpc. The other faint blue objects analyzed by Mendez & Minniti do not show any significant proper motion and are inconsistent with being halo white dwarfs; they do not contribute to the Galactic dark matter. The observed population of stars and white dwarfs is consistent with standard Galactic models.

Subject headings: dark matter — Galaxy: halo — stars: evolution — white dwarfs

1. INTRODUCTION

Faint blue objects discovered in deep *Hubble Space Telescope* (*HST*) images have been the subject of discussion in recent years. The extreme depth of the Hubble Deep Field–North (HDF-N; Williams et al. 1996) and South (HDF-S; Casertano et al. 2000) and the Hubble Ultra Deep Field (HUDF; Beckwith et al. 2003) enables us to study faint stellar objects in the regions of the color-magnitude diagram that are devoid of standard Galactic stars. Supported by the observed microlensing events toward the Large Magellanic Cloud (Alcock et al. 2000), several investigators have proposed that the faint blue objects observed in the HDF images can explain part of the dark matter in the Galaxy and that a significant population of the halo of the Galaxy may be in the form of low-luminosity white dwarfs. Claims by Mendez & Minniti (2000, hereafter MM00) that the faint blue sources in the HDF-N and HDF-S are Galactic stars seemed to be consistent with earlier findings of Ibata et al. (1999), who found five faint halo white dwarf candidates with detectable proper motions in the HDF-N. However, further analysis by Richer (2003) and Kilic et al. (2004) showed that the faint blue objects in the HDF-N do not show any significant proper motion.

A detailed analysis of the point sources in the HDF-N (Kilic et al. 2004) and the HUDF (Pirzkal et al. 2005) showed that blue extragalactic sources may be confused with white dwarfs. The (10 σ) limiting AB magnitudes of the *I*-band images for these two fields are 27.6 and 29.0, respectively. Using a 7 yr baseline, Kilic et al. (2004) obtained proper-motion measurements for the point sources in the HDF-N, including the five faint blue objects; they identified two possible disk white dwarfs, one of which now also appears spectroscopically to be a white dwarf (D. Stern 2004, private communication). Using low-resolution spectros-

copy and proper-motion measurements, Pirzkal et al. (2005) identified 20 late-type stars, 2 quasars, and 4 possible white dwarf candidates in the HUDF. Kilic et al. (2005) showed that only two of these candidates (HUDF 4839 and 9020) are firm white dwarf candidates, with HUDF 4839 possibly being a thick-disk object and HUDF 9020 being either a disk or a halo object. None of these white dwarf candidates show significant proper motion (Pirzkal et al. 2005). Nondetection of high-velocity white dwarfs in the HUDF is consistent with nondetection of halo white dwarfs in the HDF-N. Lack of detection of high-velocity white dwarfs in these two fields implies that white dwarfs account for less than 10% of the Galactic dark matter (Pirzkal et al. 2005; Kilic et al. 2005).

The discoveries by Ibata et al. (2000) and Oppenheimer et al. (2001) of apparent halo white dwarfs from kinematic surveys were enough to explain 2% of the dark matter in the solar neighborhood. On the other hand, further analysis by several investigators showed that most of these white dwarfs are associated with the thick-disk population of the Galaxy (Reid et al. 2001; Reyle et al. 2001; Bergeron et al. 2005). Nevertheless, old halo white dwarfs are observed in the globular clusters M4 (Hansen et al. 2004) and NGC 6397 (Mendez 2002) and in the field toward M4 (Kalirai et al. 2004). Reid (2005; see for a complete review on high-velocity white dwarfs) found that these observations do not require additions to the standard Galactic populations.

The HDF-S data provide another opportunity to test whether the faint blue objects in deep Hubble images can be old halo white dwarfs and whether they can explain part of the Galactic dark matter. MM00 found 22 Galactic stars and 10 faint blue objects in the HDF-S. If these 10 faint blue objects are halo white dwarfs, then they would explain 30%–50% of the dark matter in the solar neighborhood. We extend the work of Kilic et al. (2004) to the HDF-S by using the original HDF-S data and images of the same field taken 3 yr later for the GO-9267 proposal (WFPC2 Supernova Search, PI: S. Beckwith) to measure the proper motions of the point sources in the HDF-S. Section 2 describes our first-epoch data and the classification of the point sources, while data reduction procedures for our second-epoch images are discussed in § 3. Section 4 describes the proper-motion measurements for the point sources. We

---

[2] Department of Astronomy, University of Texas at Austin, 1 University Station C1400, Austin, TX 78712; kilic@astro.as.utexas.edu.
[3] Departamento de Astronomia, Universidad de Chile, Casilla 36-D, Santiago, Chile.

present our spectral energy distribution fitting results in § 5, and various implications of these results are then discussed in § 6.

2. DESCRIPTION OF THE DATA

The HDF-S was imaged using the Wide Field Planetary Camera 2 (WFPC2) and the F300W (U_{300}), F450W (B_{450}), F606W (V_{606}), and F814W (I_{814}) filters in 1998 and imaged again in 2001 using the WFPC2 and the F814W filter in order to search for high-redshift supernovae. The original images taken in 1998 reach down to AB = 26.8, 27.7, 28.3, and 27.7 in the four bands, respectively (10 σ, point source; Casertano et al. 2000). The (ver. 2) source catalogs for the first epoch are produced by the Space Telescope Science Institute (STScI) from the combined and drizzled images. Source detection was carried out on the inverse-variance-weighted sum of the F606W and F814W drizzled images. The combined F606W+F814W (hereafter $V + I$) image is significantly deeper than any of the combined images (Casertano et al. 2000).

2.1. *Identification of Point Sources*

MM00 used the stellarity index from Source Extractor (SExtractor; Bertin & Arnout 1996) to identify point sources and claimed that the star/galaxy separation is reliable for objects
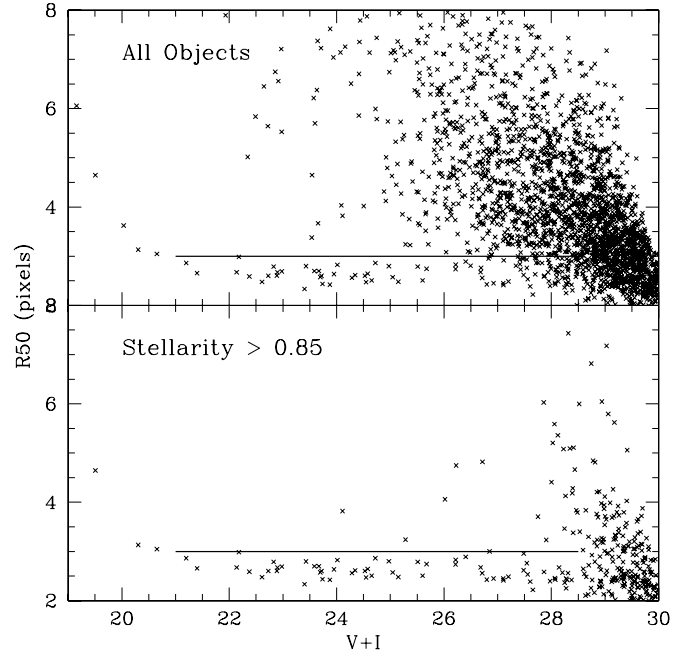

Fig. 1.—Distribution of $R50$ (half-light radius) for the HDF-S objects. The solid line separates the unresolved objects from the resolved objects.
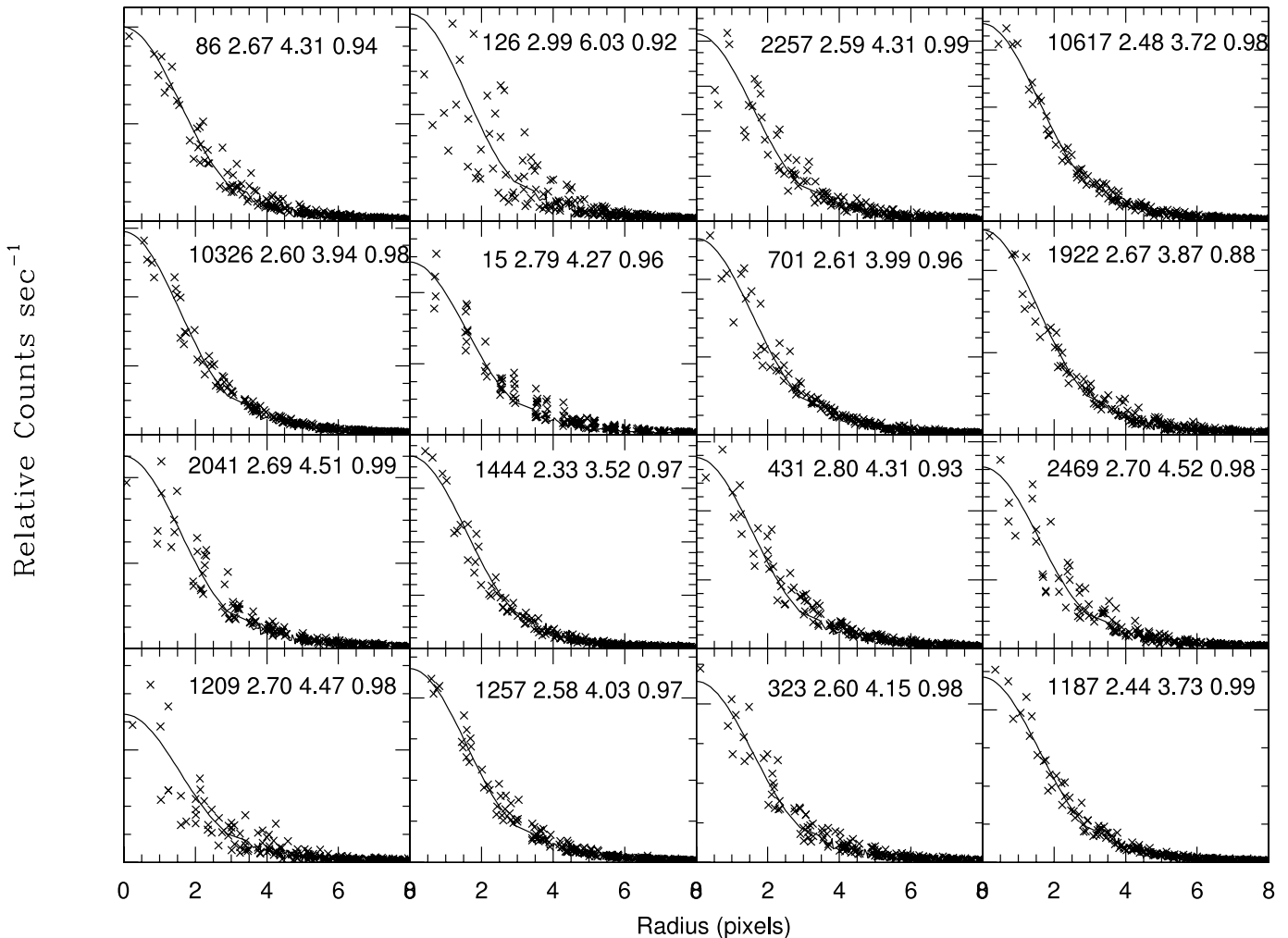

Fig. 2.—Point-spread function (PSF) distributions of the objects with $V + I > 21$, $R50 < 3$ pixels and stellarity index >0.85. The object number, $R50$, FWHM, and stellarity index of each object are shown in the top right corner of each panel. The HDFS 10617 PSF is shown in each panel for comparison.
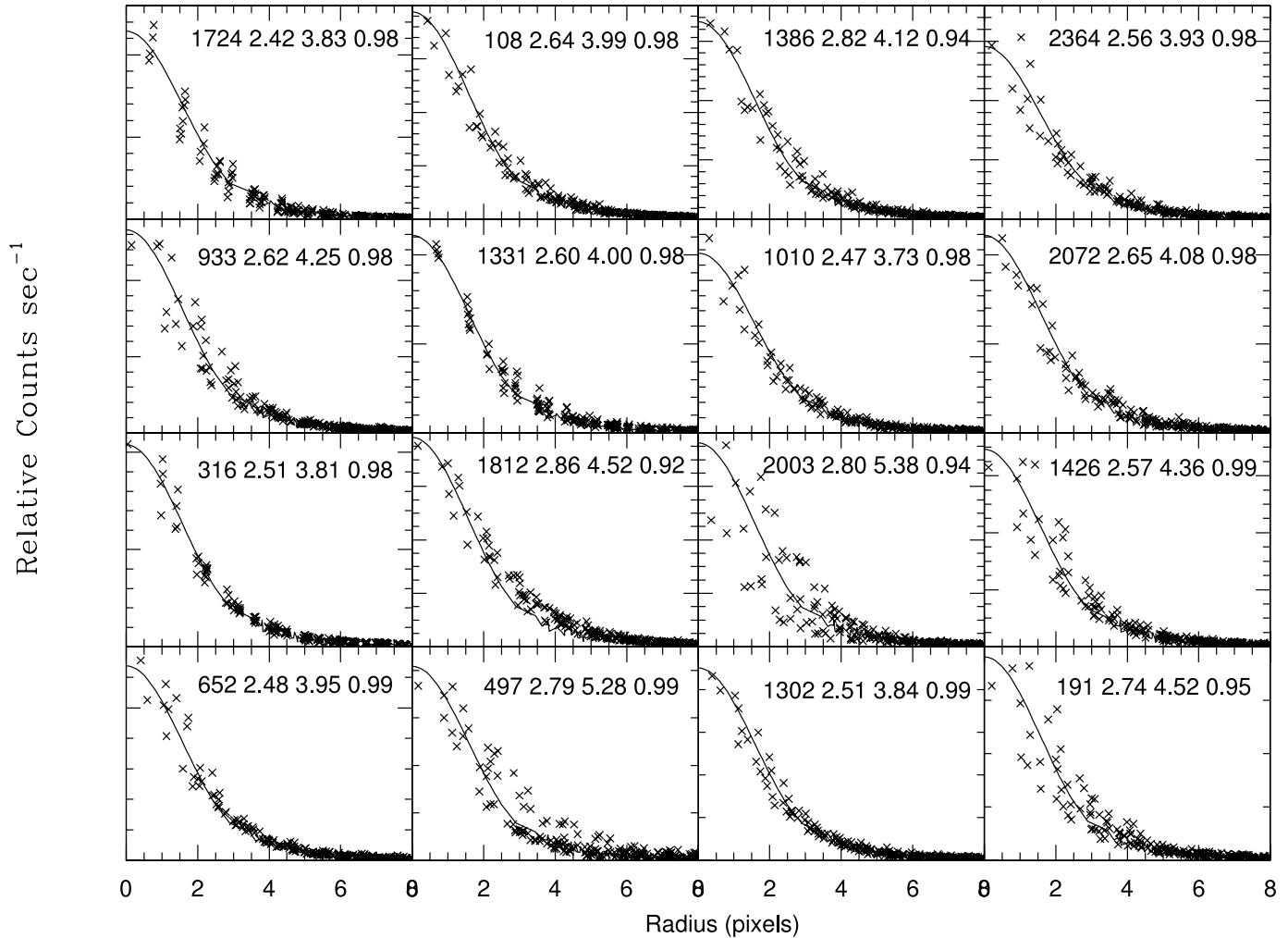
Fig. 2.—*Continued*

brighter than $V + I = 29$. They visually inspected the objects with stellarity index <0.85 and found that they are extended. MM00 identified all objects with stellarity index >0.90 as stars and found 98 point sources in 4.062 arcmin^2 of the HDF-S. They analyzed objects with $I < 27$ (15 σ detections) and found 22 late-type stars and 10 faint blue objects (see MM00 for a complete discussion).

Kilic et al. (2005) showed that the SExtractor stellarity index fails at faint magnitudes. Instead, they suggested the use of the half-light radius ($R50$) and the full width at half-maximum (FWHM) measurements, along with the empirical point-spread function (PSF) distributions, to identify the unresolved objects in deep *HST* images. Figure 1 shows the distribution of $R50$ with $V + I$ magnitude for all HDFS objects (*top*) and for the objects with the stellarity index >0.85. Objects brighter than $V + I = 20$ are saturated and therefore have higher $R50$ and lower stellarity values. It is clear from this figure that the point sources are well separated from the extended objects in this diagram down to $V + I = 28.5$. A solid line ($R50 = 3.0$) marks the separation between the resolved and the unresolved objects. We note that we trimmed the source catalog to avoid spurious detections near the detector boundaries, and we also exclude the Planetary Camera (PC) observations because the PC has a different plate scale and the PSFs are different from the PSFs for the Wide Field Cameras.

We use the IRAF task PRADPROF and the object centroids from SExtractor to plot the radial profile of each object. Our empirical PSF distributions for objects with $R50 < 3.0$, stellarity index >0.85, and $21 < V + I < 28.5$ are shown in Figure 2. As in MM00, we limit our analysis to the objects brighter than $I = 27$. The object number, $R50$, FWHM, and stellarity index of each object are shown in the top right corner of each panel. We also plot the PSF for a bright, unsaturated, unresolved source (HDFS 10617) in each panel for a direct comparison. In addition, we examined the PSF distributions for the objects with $R50 < 3.0$ and the stellarity index <0.85 and (as in MM00) found all of them to be resolved.

A comparison of the PSF for each object with our template PSF (for HDFS 10617) shows that HDFS 126 (FWHM = 6.03), 2003 (FWHM = 5.38), and 497 (FWHM = 5.28) are clearly resolved. The typical FWHM for the unresolved objects is <5. In addition, HDFS 1812, 1827, 2129, and 567 have shallower PSF distributions than the template PSF and therefore are resolved as well. Six of these seven objects have stellarity indices larger than 0.9 and therefore would be classified as point sources based on the stellarity index. Our empirical PSF distribution analysis shows that the stellarity index from SExtractor should not be used by itself to identify point sources in deep *HST* images. Instead, as Kilic et al. (2005) suggested, a combination of the $R50$, FWHM, stellarity index, and empirical PSF distributions
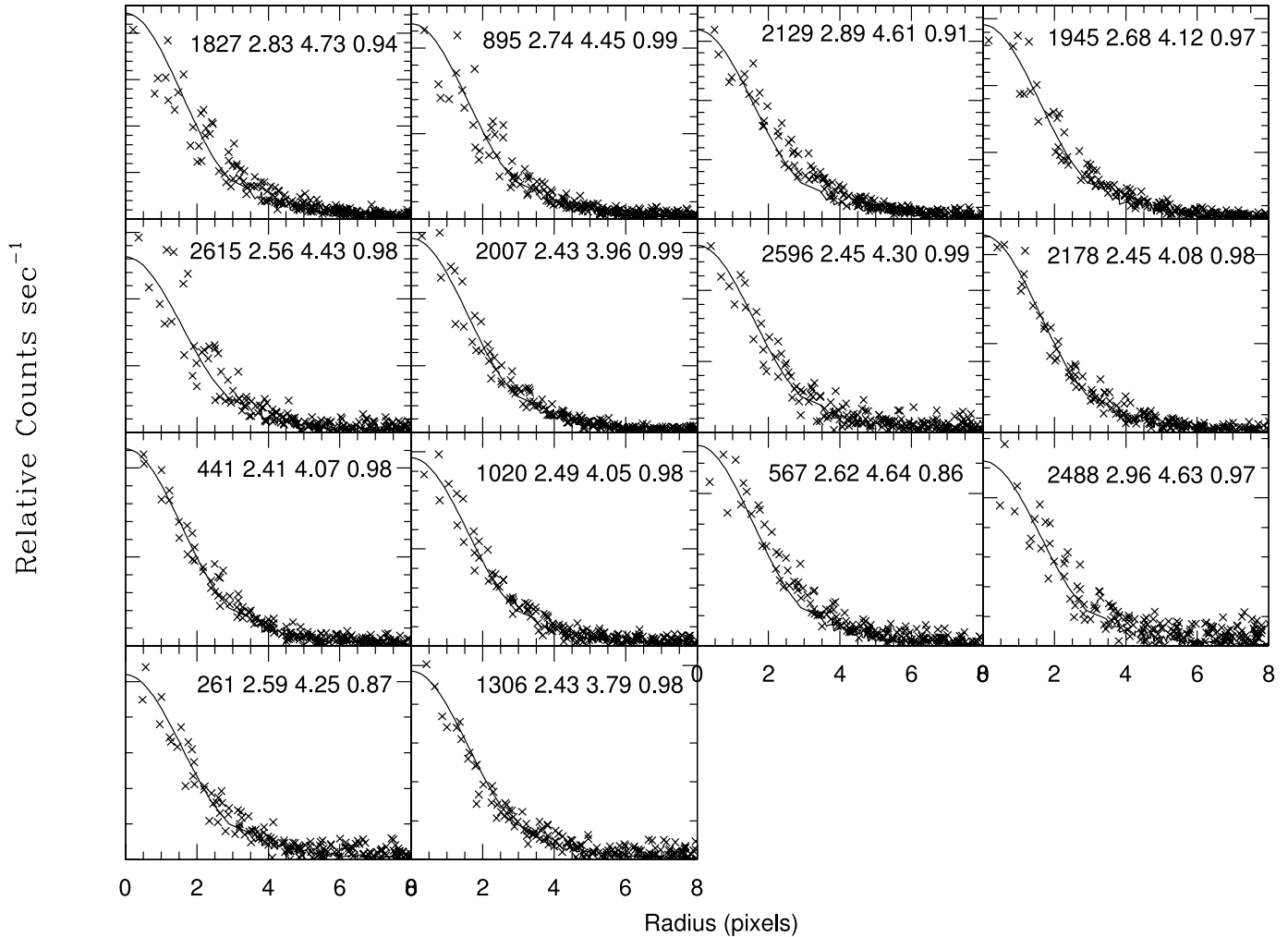
Fig. 2.—*Continued*

is required to identify unresolved objects. This analysis leaves us with 39 unresolved objects with $21 < V + I < 28.5$ and $I < 27$, plus seven brighter point sources ($V + I < 21$) in the HDF-S.

We note that we may have a few barely resolved objects in our sample, e.g., HDFS 191. Some extragalactic sources, e.g., luminous compact blue galaxies (LCBGs), can be quite small (half-light radius 1–3 kpc) and blue ($B - V < 0.6$; Werk et al. 2004). Nevertheless, *HST* is able to resolve almost every galaxy if a high enough signal-to-noise ratio is obtained. For example, Hoyos et al. (2004) could resolve four LCBGs at intermediate redshifts ($z = 0.1$–0.44, $R50 = 0.7$–2.7 kpc) using WFPC2 ($R50 = 0''23$–$0''47$). In addition, using low-resolution spectroscopy from the GRAPES survey, Pirzkal et al. (2005) showed that none of the unresolved objects in the HUDF ($I < 27$) are LCBGs. Therefore, the number of compact galaxies that are classified as unresolved should be small. Even if our sample is contaminated by a few faint resolved objects, misclassification of these objects would not change the conclusions derived from our analysis (see § 7).

Figure 3 shows the distribution of the $R50$ and the FWHM for the HDF-S objects in different magnitude ranges. Objects with stellarity index >0.85 are shown as filled triangles, and the unresolved objects identified from their PSF distributions are shown as filled circles. All of the unresolved objects ($V + I > 21$) have stellarity index >0.87, $R50 < 3$, and FWHM < 5. It is clear from

this figure that the unresolved objects can be identified easily down to $V + I = 27$. Although the classification becomes harder for $V + I > 27$, five of the six objects that are fainter than $V + I = 27$ and classified as unresolved (HDFS 261, 441, 1020, 1306, and 2178) all have PSFs, $R50$, FWHM, and stellarity values consistent with unresolved objects. Therefore, their identification as point sources is secure. The identification of HDFS 2488 ($R50 = 2.96$, $I = 26.97$) as unresolved is questionable, but this object is still included in our analysis for completeness purposes. Astrometric and photometric data for the 46 objects that we identified as unresolved are given in Table 1. We adopted the calibrated photometry of Casertano et al. (2000).

3. THE SECOND-EPOCH DATA

The second-epoch data consist of 36 1200 s images in the F814W filter and provide a baseline of 3 yr. The 10 σ limiting magnitude for the point sources in the combined second-epoch image is AB = 26.7.

3.1. *Data Reduction*

We followed the reduction steps outlined in the *HST* dither handbook (Koekemoer et al. 2002) to reduce the second-epoch data. All 36 images were processed with a procedure that included the following steps: initial pipeline processing, sky background subtraction, cross-correlation and finding the offsets between
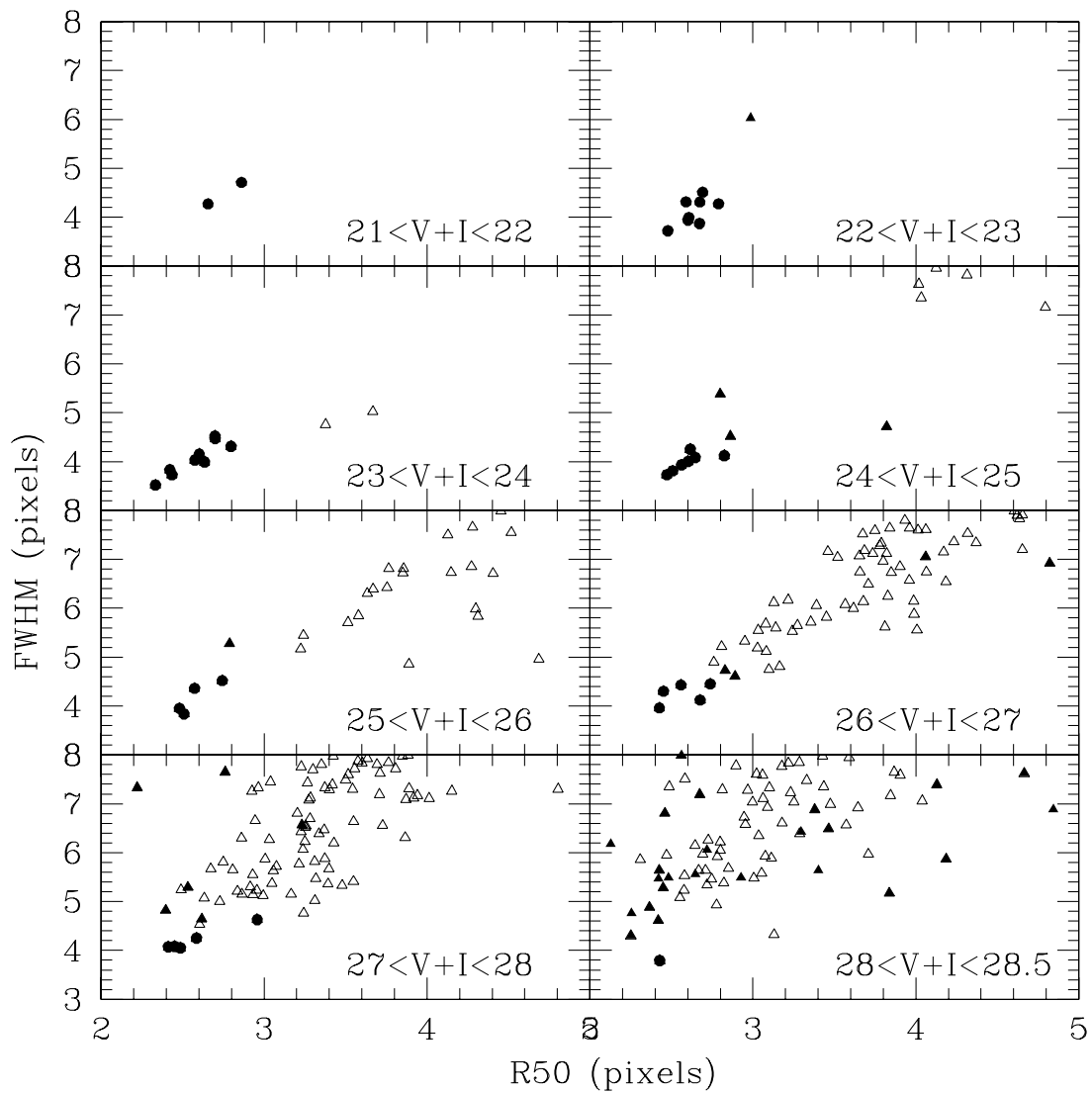
FIG. 3.—Relation between $R50$ and FWHM for the HDFS objects in different magnitude ranges. Objects with stellarity index >0.85 are shown as filled triangles, whereas the open triangles show the rest of the objects in the HDFS catalog. Filled circles represent unresolved objects identified from their empirical PSF distributions. Point sources can be identified easily down to $V + I = 27$, and the star/galaxy sequences begin to blur for $V + I > 27$.

TABLE 1
POINT SOURCES IN THE HUBBLE DEEP FIELD SOUTH

| No.	Object	X (HDFS)	Y (HDFS)	U_{300}	B_{450}	V_{606}	I_{814}	Stellarity
10663..........................	J223250.50−603400.8	3039.857	884.384	23.43	19.90	19.13	18.20	0.72
10692..........................	J223257.00−603405.7	1836.189	772.533	20.89	19.14	19.22	18.61	0.94
10017..........................	J223254.90−603144.1	2255.468	4321.344	24.99	21.47	20.26	18.75	0.78
10666..........................	J223305.04−603400.8	350.133	907.811	25.62	21.80	20.52	19.24	0.99
10151..........................	J223250.51−603218.8	3059.869	3445.525	21.76	20.25	20.35	19.87	0.99
10081..........................	J223247.45−603160.0	3632.237	3911.988	27.14	23.93	22.23	19.89	0.89
1576..........................	J223303.65−603330.6	614.027	1664.433	28.93	23.45	21.92	20.23	0.98
2257..........................	J223305.63−603358.2	242.259	974.553	. . .	24.50	22.87	21.15	0.99
10617..........................	J223258.30−603351.7	1599.243	1127.375	29.19	25.26	23.55	21.36	0.98
86..............................	J223248.06−603148.6	3521.148	4199.046	23.98	22.24	21.76	21.46	0.94
15..............................	J223248.47−603139.3	3447.529	4431.511	27.51	24.78	23.28	21.59	0.96
2041..........................	J223251.03−603353.5	2942.939	1069.948	28.28	25.97	24.16	21.68	0.99
10326..........................	J223252.60−603259.5	2664.651	2425.551	27.64	24.45	22.87	21.71	0.98
701..........................	J223251.33−603237.6	2903.785	2973.677	29.04	24.80	23.24	21.78	0.96
1922..........................	J223247.58−603347.3	3583.103	1217.824	. . .	24.67	23.05	21.87	0.88
1209..........................	J223245.74−603309.7	3931.750	2158.995	. . .	26.93	24.75	22.24	0.98
1257..........................	J223256.68−603313.8	1906.621	2075.463	. . .	26.21	24.56	22.46	0.97
431..........................	J223247.94−603216.6	3537.732	3496.018	25.68	23.69	23.14	22.69	0.93
1187..........................	J223258.46−603307.7	1578.305	2231.191	28.61	25.28	23.79	22.74	0.99
2469..........................	J223253.24−603413.4	2529.645	574.651	26.26	23.89	23.22	22.83	0.98
323..........................	J223246.71−603207.2	3765.987	3728.892	26.20	24.07	23.41	22.97	0.98
108..........................	J223249.34−603149.0	3284.156	4189.406	27.78	25.54	24.01	22.97	0.98
1444..........................	J223258.77−603323.5	1517.394	1833.822	23.30	22.69	22.80	23.02	0.97
2364..........................	J223257.72−603408.7	1702.207	699.988	28.80	27.21	25.31	23.04	0.98
1724..........................	J223258.11−603337.4	1637.423	1485.485	26.72	24.26	23.60	23.12	0.98
1386..........................	J223248.36−603319.0	3444.716	1930.820	28.01	24.99	23.86	23.16	0.94
933..........................	J223247.94−603251.1	3528.871	2630.077	. . .	26.35	24.75	23.24	0.98
2072..........................	J223255.36−603355.0	2142.223	1039.552	27.33	26.90	25.45	23.31	0.98
1331..........................	J223247.05−603316.0	3687.492	2003.460	28.08	26.35	24.68	23.50	0.98
316..........................	J223253.09−603206.7	2584.979	3752.969	29.53	26.00	24.57	23.75	0.98
1010..........................	J223256.14−603256.9	2011.083	2498.703	27.27	24.84	24.23	23.78	0.98
1426..........................	J223304.54−603322.5	450.919	1867.914	30.99	26.48	25.04	24.10	0.99
652..........................	J223251.18−603234.0	2933.967	3064.594	28.54	26.14	24.98	24.30	0.99
191..........................	J223256.17−603156.5	2018.212	4011.988	. . .	28.28	26.82	24.41	0.95
1302..........................	J223252.60−603315.1	2661.049	2035.617	. . .	27.28	25.58	24.66	0.99
895..........................	J223246.22−603248.4	3847.227	2693.725	28.08	26.20	25.77	25.57	0.99
2615..........................	J223258.88−603421.9	1485.890	368.651	25.45	25.17	26.91	25.69	0.98
1945..........................	J223249.59−603347.7	3211.154	1212.031	26.23	26.53	26.46	25.88	0.97
2007..........................	J223249.63−603351.3	3201.802	1122.227	29.13	28.72	26.69	25.92	0.99
2596..........................	J223254.05−603419.4	2378.829	425.350	. . .	27.73	26.89	26.00	0.99
441..........................	J223255.01−603217.7	2228.504	3480.124	29.78	28.34	27.12	26.14	0.98
1020..........................	J223254.03−603257.4	2400.755	2481.265	29.20	28.83	27.12	26.29	0.98
2178..........................	J223258.94−603400.1	1478.979	917.399	28.73	28.41	26.71	26.47	0.98
261..........................	J223248.69−603200.8	3402.451	3893.844	31.80	28.74	27.86	26.91	0.87
1306..........................	J223258.20−603315.2	1625.787	2040.621	29.73	. . .	28.47	26.93	0.98
2488..........................	J223245.71−603413.4	3922.570	561.776	28.20	26.45	26.65	26.97	0.97
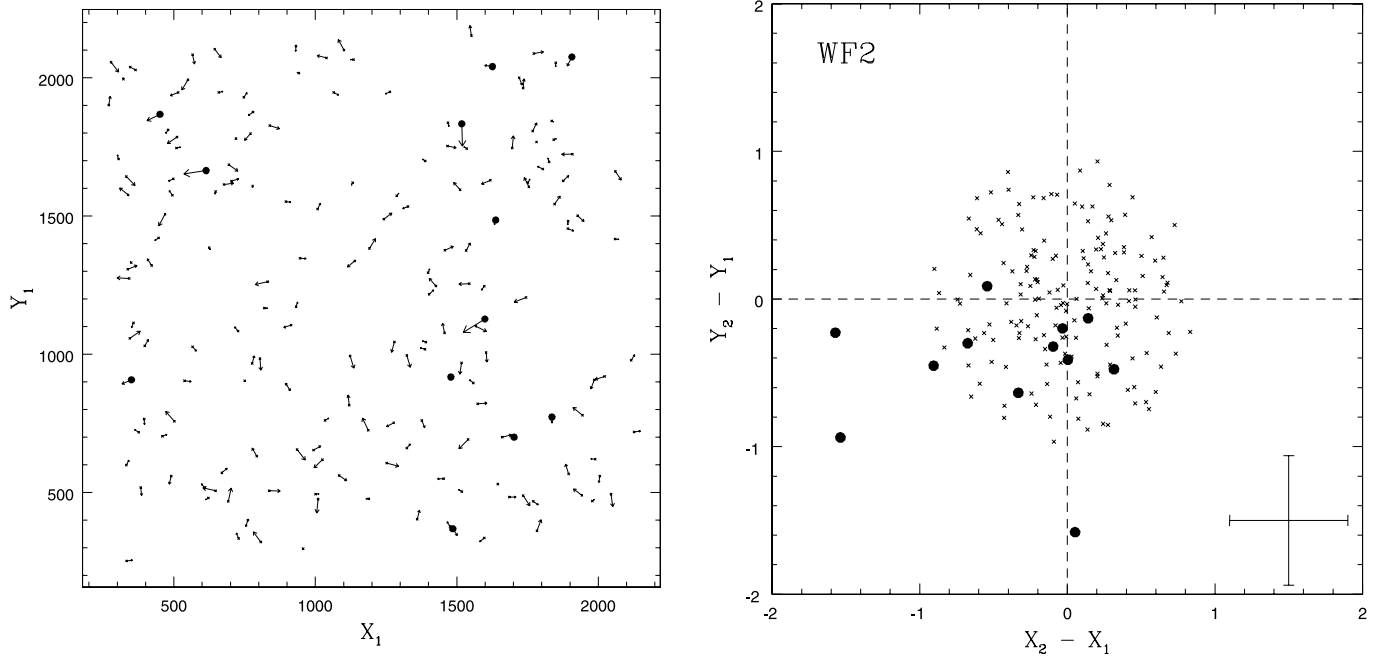
Fig. 4.—*Left*, Observed shifts (scaled by a factor of 50) of point sources (*circles*) and surrounding reference compact objects (*crosses*) in the HDFS WF2 chip between epoch 1 and epoch 2 images; *right*, differences between the first-epoch coordinates (X_1, Y_1) and the transformed second-epoch coordinates (X_2, Y_2) for the same objects. The expected scatter caused by the transformation itself is represented by the error bar in the lower right corner of the figure. The units on the axes are HDFS pixels (0″.04 pixel^{-1}).

images, cosmic-ray rejection, scattered-light correction, and final drizzling and combination.

We obtained the standard pipeline processed images of the HDFS 2001 observations from the Space Telescope Science Institute Web site. After subtracting the sky background from each image, cosmic rays were removed so that cross-correlation would not be affected by them. Each image is cross-correlated with the first image (reference image) in order to determine the shifts between them. Most hot pixels, i.e., pixels with elevated dark current, can be identified easily with images taken in different dither positions. Nevertheless, some hot pixels may escape detection if they fall near an object. We use the static pixel mask reference file, used in pipeline calibration, to create a bad-pixel mask for our images.

The cosmic-ray rejection is done in three steps. Each individual input image is registered and drizzled to the same output frame. Ten of the 36 images have a higher background and suffer from a distinctive cross-shaped pattern due to the shadowing of the *HST* secondary by the support structure of the WFPC2 repeater (Casertano et al. 2000). The 26 images without the scattered-light problem are combined into a single cosmic-ray–free median image for each chip. The median image is then blotted back (reverse drizzling) to the original position of each input image. Images with the cross pattern were corrected by applying a median filter to the image obtained after subtracting the expected image produced by the BLOT task. Inspection of the resulting images showed that the subtraction works well. In additon, each image is compared with the blotted images to identify and mask cosmic rays and bad pixels.

The final drizzled images are constructed by applying the shifts and the mask files to the individual images and are combined into a single image for each WFPC2 chip. The parameters chosen for the final drizzling were similar to those used for the HDFS 1998 images. We used a footprint area of 0.6 input pixels (0.5 for the HDFS 1998 images), and a pixel scale of 0.4 pixels, resulting in a linear scale of 0″.04 pixel^{-1}. Our experimenta-

tion with different values of the footprint for the drizzling algorithm showed that image statistics are better for a footprint of 0.6 pixels. Because of the relatively small pointing shifts, we decided not to combine all images into a single mosaic comprising all four WFPC2 chips. The pointing shifts are not large enough to recover the part of the sky that is lost between the WFPC2 chips.

3.2. *Object Identification*

Casertano et al. (2000) used the SExtractor package to create source catalogs for the HDF-S 1998 images. We have created source catalogs for the second-epoch data using SExtractor, version 2.3, with the same parameters as used for the HDF-S original images. Our main incentive for using SExtractor was its incorporation of weight maps in modulating the source detection thresholds. SExtractor follows a standard connected-pixel algorithm for source identification. We set the source detection threshold to 0.65 and the minimum area to 16 drizzled pixels. We convolve the image with a Gaussian (FWHM = 3 pixels), and sources with 16 pixels above the detection threshold are included in our catalog. Only those objects matching the positions of the objects in the first-epoch data with differences less than 1 pixel (0″.04) are included in our final catalog. Furthermore, we visually inspected all of these sources to avoid any mismatches. We note that the 1 pixel limit is only used for the reference compact objects, as we do not impose any limits on the proper motion of the point sources.

4. PROPER-MOTION MEASUREMENTS

The original HDF-S images were corrected for distortion by Casertano et al. (2000). The drizzling procedure that we used to reduce our second-epoch data also corrects for distortion with standard procedures outlined in the *HST* dither handbook. Even with these corrections, however, some distortion remains (Bedin et al. 2003). Kilic et al. (2004) and Pirzkal et al. (2005)
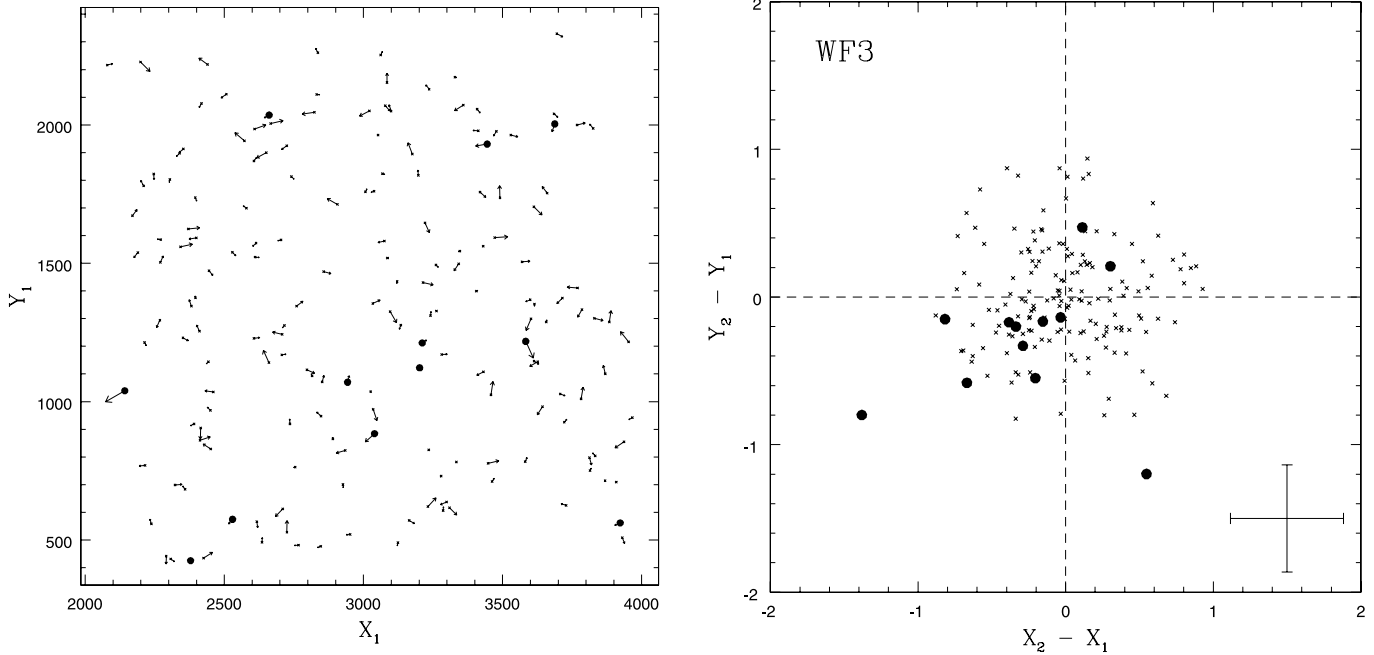
FIG. 5.—Same as Fig. 1, but for the objects detected in WF3.

showed that a simple quadratic transformation can be used to improve the correction for distortion in the WFPC2 and the Advanced Camera for Surveys (ACS) images, respectively.

To select reference objects, we use all of the compact objects (isolated, low residuals, and not fuzzy) with positional differences less than 1 pixel (0″04) between the two epochs to derive a quadratic (third-order, two-dimensional polynomial) transformation for each chip (WF2, WF3, and WF4). We rejected deviant points using a 3 σ rejection algorithm. This rejection is required because our reference objects are compact galaxies and centroiding errors are larger for galaxies. Even though using a local transformation for each object can increase the accuracy

of our proper-motion measurements, some of the point sources are near the edges of the chip; therefore it is not possible to perform a local transformation for each object. Our transformation solutions for individual chips are still better than doing a global transformation using a single mosaic image. After mapping the distortions with the GEOMAP package, coordinates for the compact objects and the point sources were transformed to the second-epoch positions with the GEOXYTRAN routine.

Figures 4, 5, and 6 show the observed shifts (scaled by a factor of 50) of each object on WF2, WF3, and WF4, respectively. Crosses represent reference compact objects, and circles represent the point sources identified in the previous section. The
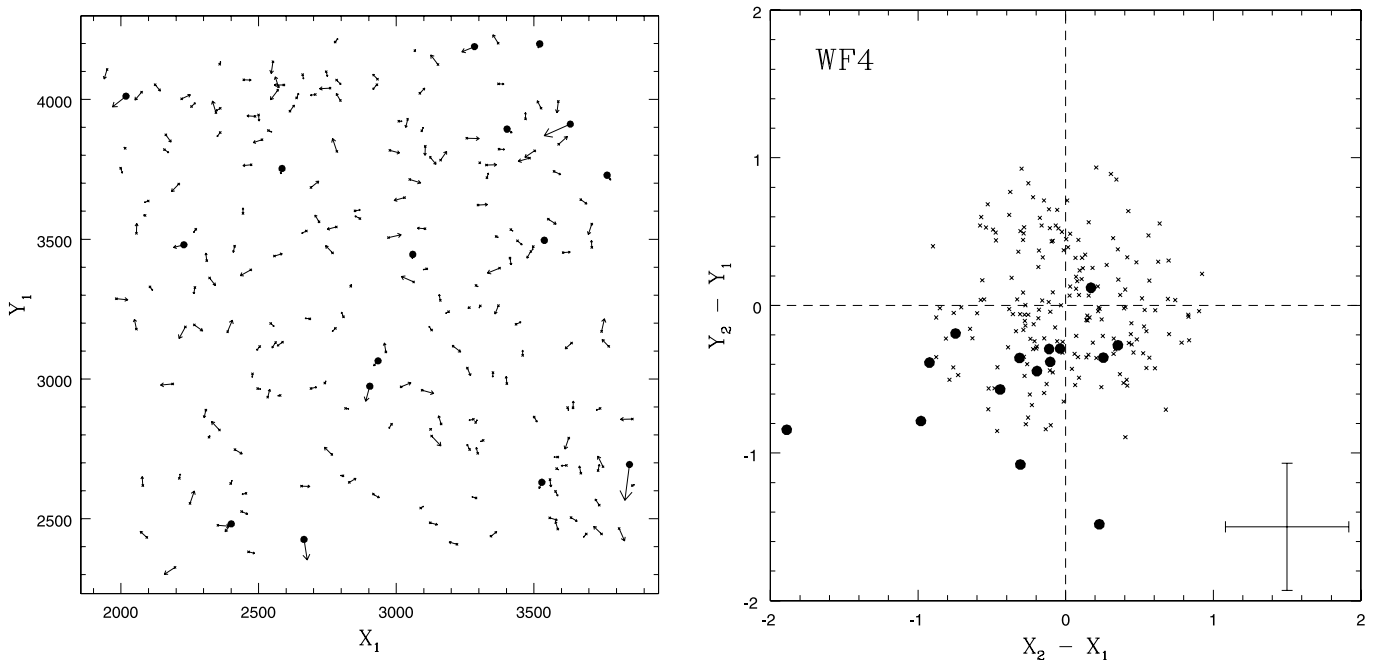
FIG. 6.—Same as Fig. 1, but for the objects detected in WF4.

TABLE 2
PROPER MOTIONS

Object	Chip	μ_x (pixel)	μ_y (pixel)	μ (mas yr^{-1})	σ_μ (mas yr^{-1})	μ/σ
10663........	wf3	−0.67	−0.58	11.82	7.04	1.68
10692........	wf2	0.00	−0.41	5.50	7.93	0.69
10666........	wf2	−0.68	−0.30	9.85	7.93	1.24
10151........	wf4	−0.04	−0.29	3.94	8.00	0.49
10081........	wf4	−1.89	−0.84	27.58	8.00	3.44
1576..........	wf2	−1.57	−0.23	21.17	7.93	2.67
10617........	wf2	−1.54	−0.94	24.01	7.93	3.03
86..............	wf4	−0.11	−0.30	4.21	8.00	0.53
2041..........	wf3	0.11	0.47	6.47	7.04	0.92
10326........	wf4	0.23	−1.48	20.00	8.00	2.50
701............	wf4	−0.31	−1.08	14.94	8.00	1.87
1922..........	wf3	0.55	−1.20	17.57	7.04	2.50
1257..........	wf2	−0.33	−0.64	9.56	7.93	1.21
431............	wf4	0.17	0.12	2.79	8.00	0.35
2469..........	wf3	−0.29	−0.33	5.86	7.04	0.83
323............	wf4	0.26	−0.35	5.83	8.00	0.73
108............	wf4	−0.92	−0.39	13.33	8.00	1.67
1444..........	wf2	0.05	−1.58	21.07	7.93	2.66
2364..........	wf2	−0.03	−0.20	2.70	7.93	0.34
1724..........	wf2	−0.10	−0.32	4.48	7.93	0.56
1386..........	wf3	−0.82	−0.15	11.07	7.04	1.57
933............	wf4	−0.19	−0.44	6.47	8.00	0.81
2072..........	wf3	−1.38	−0.80	21.28	7.04	3.02
1331..........	wf3	−0.21	−0.55	7.83	7.04	1.11
316............	wf4	−0.10	−0.38	5.29	8.00	0.66
1426..........	wf2	−0.91	−0.45	13.50	7.93	1.70
652............	wf4	−0.31	−0.36	6.32	8.00	0.79
191............	wf4	−0.98	−0.78	16.73	8.00	2.09
1302..........	wf3	−0.34	−0.20	5.22	7.04	0.74
895............	wf4	−0.34	−2.60	34.90	8.00	4.36
2615..........	wf2	0.32	−0.48	7.62	7.93	0.96
1945..........	wf3	0.30	0.21	4.91	7.04	0.70
2007..........	wf3	−0.15	−0.17	3.03	7.04	0.43
2596..........	wf3	−0.03	−0.14	1.90	7.04	0.27
441............	wf4	−0.75	−0.19	10.27	8.00	1.28
1020..........	wf4	−0.44	−0.57	9.63	8.00	1.20
2178..........	wf2	0.14	−0.13	2.56	7.93	0.32
261............	wf4	0.35	−0.27	5.94	8.00	0.74
1306..........	wf2	−0.54	0.09	7.34	7.93	0.93
2488..........	wf3	−0.38	−0.17	5.60	7.04	0.80

NOTE.—HDFS 15, 1010, 1187, 1209, 2257, and 10017 are out of the field of view in the second-epoch data.

FIG. 7.—Observed shifts of all point sources in the HDF-S. The directions of increasing Galactic longitude (l) and latitude (b) and the south Galactic pole (SGP) are also shown.

Figure 7 shows the observed shifts of all point sources along with the Galactic coordinates. Halo objects rotate around the Galactic center more slowly than disk stars such as the Sun. Solar motion relative to the halo objects corresponds to a speed of ~200 km s^{-1} in the direction $l = 90°$, $b = 0°$ (Mihalas & Binney 1981). Therefore, halo objects are expected to lag behind the disk objects in the direction opposite to the rotation direction of the Sun (l). A comparison of Figures 4, 5, 6, and 7 shows that even though the reference compact objects show a symmetric distribution around the origin, most of the point sources in the HDF-S are located in the lower left quadrant of the figure; the majority of them lag behind the Sun and therefore are likely to be halo objects.

Halo stars are expected to have large proper motions as a result of their high velocities relative to the Sun. MM00 claimed that the faint blue objects in the HDF-S could be ancient halo white dwarfs with distances, based on consistency with white dwarf absolute magnitudes, less than about 2 kpc from the Sun. Assuming $V_{\rm tan} = 200$ km s^{-1} for a halo star at a distance ≤ 2 kpc, we would expect to measure a proper motion of ≥ 21 mas yr^{-1} for the faint blue objects. Nine of the faint blue objects identified by MM00 (HDFS 1812, 1827, 1945, 2007, 2178, 441, 1020, 261, and 1332) have proper motions in the range 2.26–10.27 mas yr^{-1} and therefore are not likely to be halo white dwarfs. The remaining object, HDFS 1444, exhibits a significant proper motion, 21.07 ± 7.93 mas yr^{-1}, and is likely to be either a thick disk or a halo object. If the majority of these faint blue objects are not halo white dwarfs, what are they?

5. SPECTRAL ENERGY DISTRIBUTION FITTING

It is always desirable to obtain spectroscopy of starlike objects to distinguish quasars from stars and also to determine the spectral types of stars in order to have a reliable estimate of their absolute magnitudes and kinematic properties. Unfortunately, the most interesting point sources in deep Hubble images are the faintest and therefore the hardest ones for which to obtain

transformation error bars are shown in the right panel of each figure. It is clear from these figures that the reference objects do not show any systematic motion, and several point sources are statistically well separated from the reference objects; they are moving with respect to this external reference frame.

4.1. Results

Our proper-motion measurements for the point sources in the HDF-S and their significances (μ/σ) are given in Table 2. Typical errors in our measurements are 7–8 mas yr^{-1}. Hence, only those objects having proper motions larger than 15 mas yr^{-1} have significance greater than 2 σ. Our errors in proper-motion measurements are larger than that of Kilic et al. (2004) due to the fact that the time difference between the first- and second-epoch images is only 3 yr, versus 7 yr in that study. There are nine point sources with $\mu/\sigma \geq 2$ in our sample, and four of these stars (HDFS 10081, 10617, 2072, and 895) display significant ($\mu/\sigma \geq 3$) proper motion.
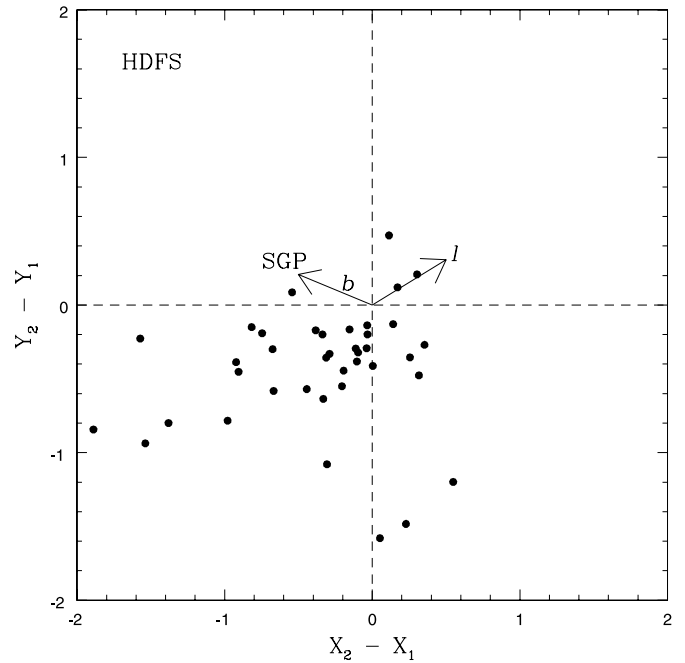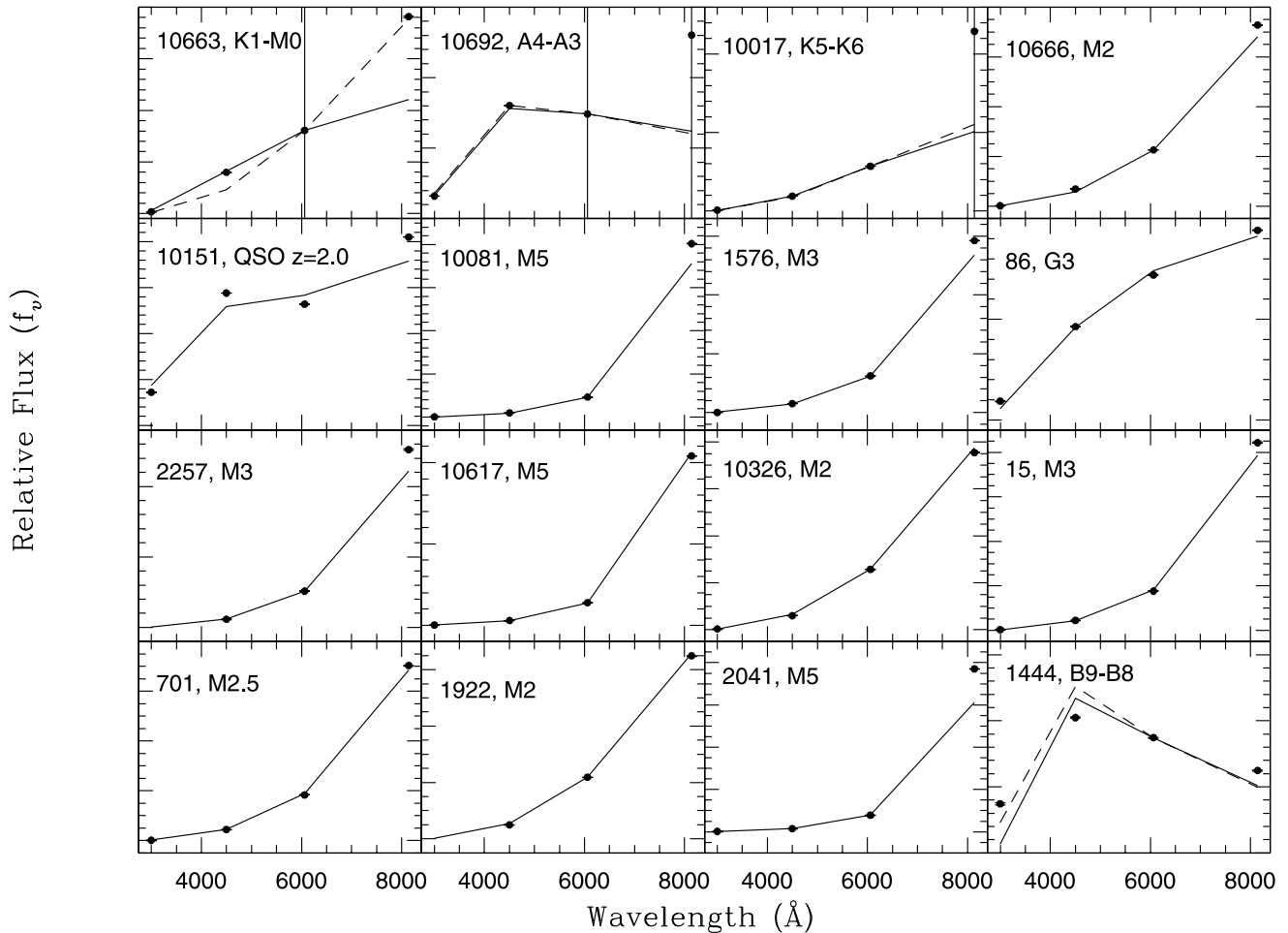
Fig. 8.—Spectral energy distribution and best-fitting template for the point sources in the HDF-S.

spectroscopy. There is only one deep field, the HUDF, that is studied spectroscopically to very faint magnitudes ($I \leq 27$; Pirzkal et al. 2005). Pirzkal et al. (2005) found 28 point sources in the HUDF, including two quasars (and two more quasars with $I > 27$). Even though spectroscopy is superior to spectral energy distribution (SED) fitting using photometry, Kilic et al. (2005) could identify the quasars and the stars in the HUDF from their photometry. Using the IRAF package CALCPHOT, which is designed for simulating the *HST* observations, Kilic et al. (2005) showed that SED fitting can be used to identify quasars and to assign spectral types to stars. Their classifications for the stars agreed reasonably well with the Pirzkal et al. (2005) spectroscopic classifications, and they were also able to predict the redshifts of two of the quasars correctly, whereas the other two were predicted to be at lower redshifts than the spectroscopic redshift measurements.

Here we adopt the same SED-fitting procedures used by Kilic et al. (2005). We use the Pickles (1998) stellar templates and the composite-quasar spectrum from the Sloan Digital Sky Survey (SDSS; Vanden Berk et al. 2001) to simulate SEDs in U_{300}, B_{450}, V_{606}, and I_{814} using the CALCPHOT task. Our simulations include stellar templates from O5 to M6 dwarf stars, and the composite-quasar spectrum is used to simulate the colors for quasars up to $z = 4.8$. Note that we do not simulate the colors of the broad range of galaxy types, as almost every galaxy with sufficient signal-to-noise ratio is resolved by *HST* (e.g., 2 kpc at $z = 0.5$ projects to $0''33$ for $\Omega_0 = 0.3$, $\Lambda_0 = 0.7$, and $H_0 = 70$).

The observed magnitudes for the faint blue objects are converted to F_ν, normalized at V_{606}, and compared with our simulated SEDs. We assign spectral types to each object using a χ^2 minimization technique. Each photometry point is weighted according to its error bar, but we also tried giving equal weight to each photometric band to explore possible fits. Figure 8 shows our best-fit solutions to the point sources in the HDF-S. Observed fluxes are shown as circles, the solid lines show the best-fit stellar or quasar templates when each photometric band is weighted according to its error bar, and the dashed lines show the best-fit templates, assuming equal weights for all bands. The object number and the assigned spectral types are given in the top left corner of each plot. Error bars for the observed fluxes are so small that they can only be seen for the fainter objects. We note that the U and B photometry for HDFS 2615 is probably wrong, as it is barely detected in the U and B images, yet its photometry shows excesses in the U and the B filters, also apparent in Figure 13. Even though our SED-fitting algorithm gives a range of spectral types (O9–M2) for this object, it is more likely to be an M-type star, based on more accurate V and I photometry.

Figure 8 shows that there are four pointlike sources with SEDs better explained by quasars than stars. HDFS 10151 ($z = 2.0$), 1945 ($z = 0.2$), 2007 ($z = 4.7$), and 2178 ($z = 4.0$) have colors more consistent with being quasars. Interestingly enough, three of these objects were classified as possible halo white dwarf candidates by MM00. These four objects have proper motions in the
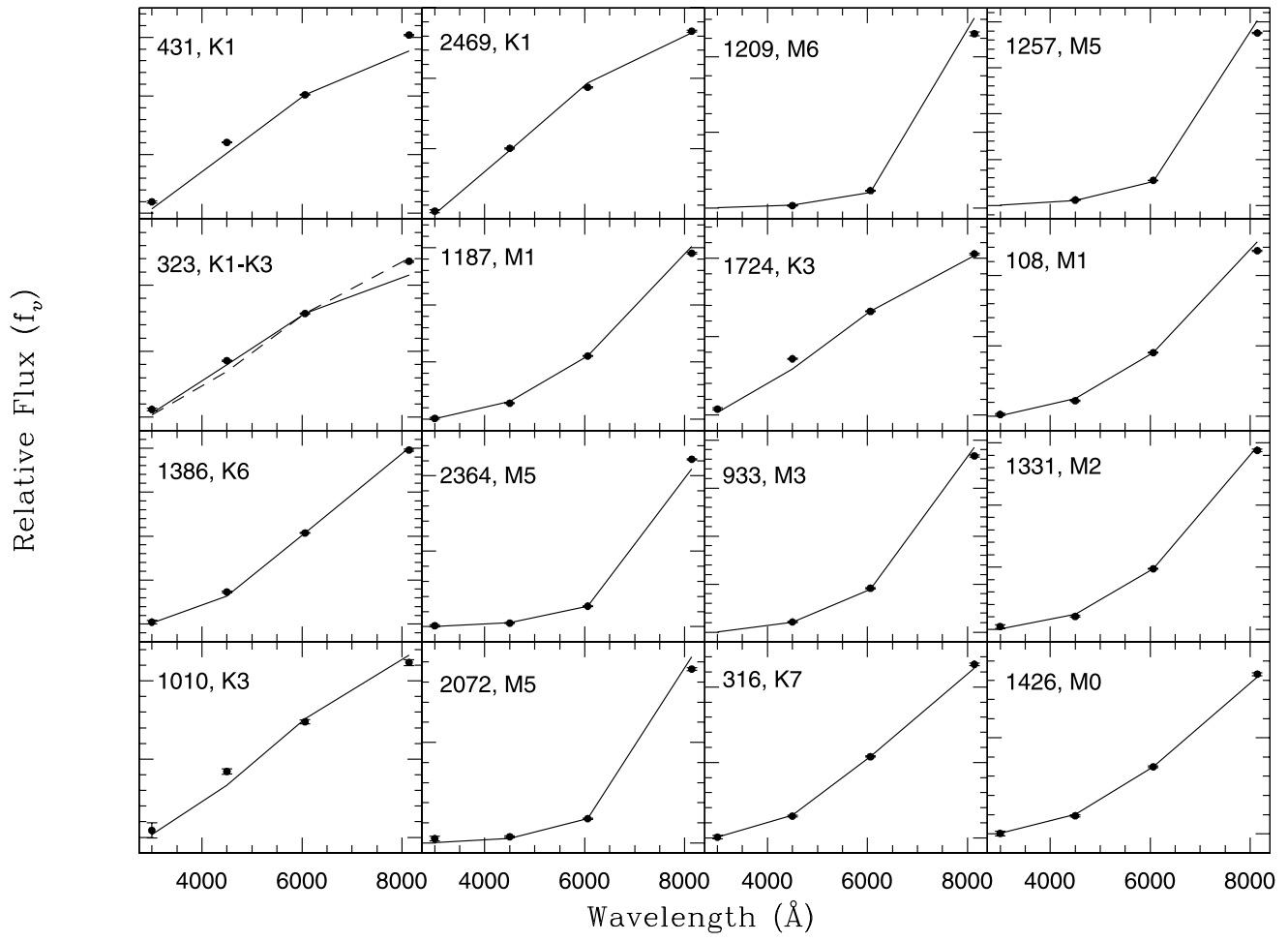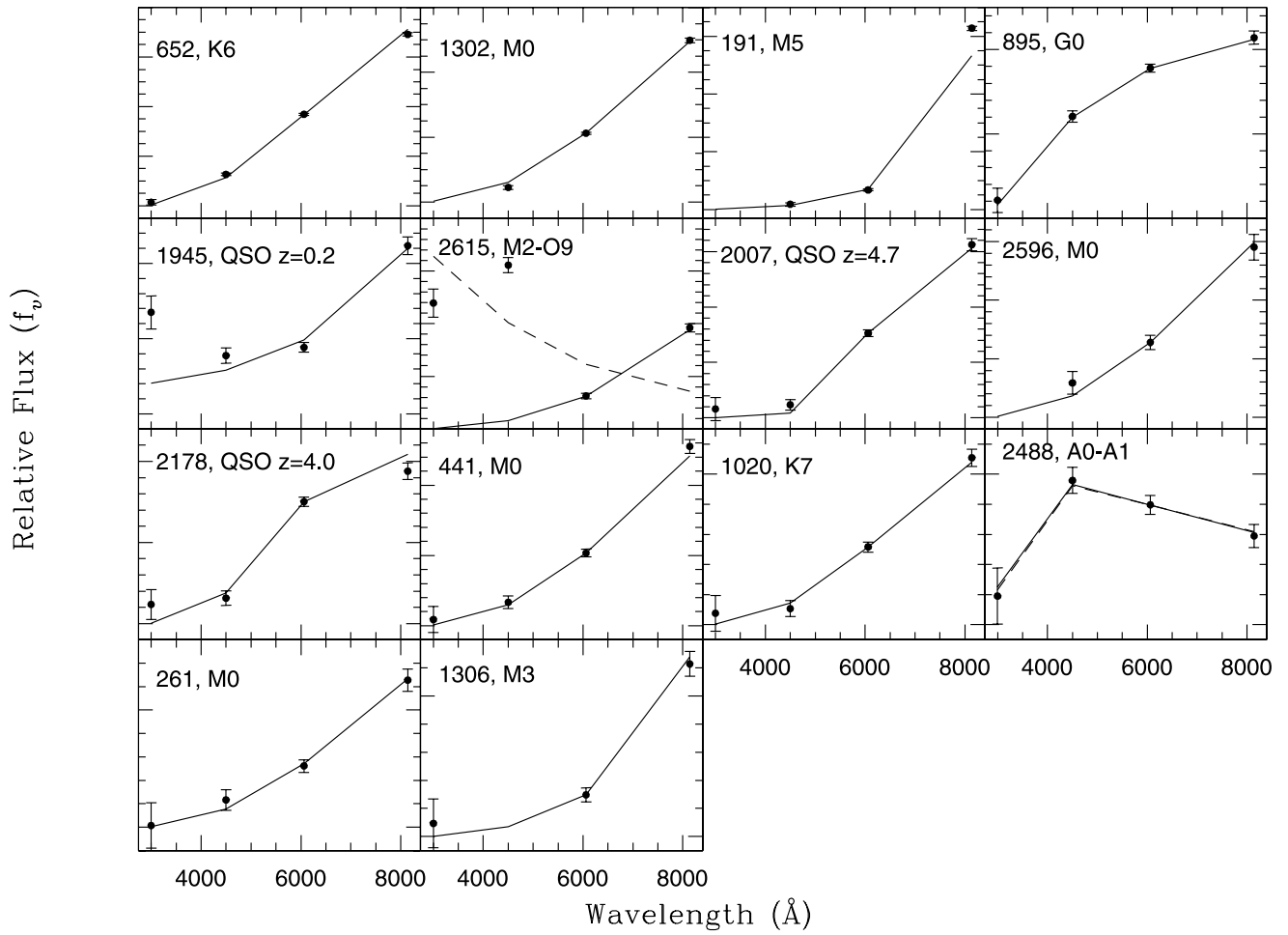
FIG. 8.—*Continued*

Relative Flux (f_ν)

Wavelength (Å)

652, K6

1302, M0

191, M5

895, G0

1945, QSO z=0.2

2615, M2-O9

2007, QSO z=4.7

2596, M0

2178, QSO z=4.0

441, M0

1020, K7

2488, A0-A1

261, M0

1306, M3

FIG. 8.—*Continued*

6. DISCUSSION

We identified four quasars and 42 stars, including 36 K0 or later type stars, with our SED-fitting technique. We adopt the absolute magnitude (M_V) for each spectral type from Pickles (1998; Table 2). We use the M_V for each object to simulate the absolute magnitudes in the WFPC2 F606W filter (M_{F606W}). We calculated photometric distances for all of the objects in our sample using the simulated M_{F606W} and the observed V_{606} magnitudes. Combining our proper-motion measurements with photometric distances, we are able to derive tangential velocities for the stars. The photometric errors for the point sources in the HDF-S are small; hence they cause only relatively small errors in the estimated distances. On the other hand, if the assigned spectral types are wrong by 1 index (for example, M3 instead of M2), then the absolute magnitudes could be wrong by as much as 1 mag. We also note that our stellar templates have approximately solar metallicity. Therefore, the distances to the metal-poor halo objects, which are intrinsically fainter for the same spectral type, may be overestimated by our SED-fitting method. For example, a metal-poor G0 dwarf ([Fe/H] $= -0.8$) would be 0.5 mag fainter than a solar metallicity G0 star (Pickles 1998). Hence, the distance to a metal-poor G0-type star would be overestimated by 26%.

In order to determine the effect of different metallicites, we use synthetic spectra from a PHOENIX model atmosphere grid (Brott & Hauschildt 2005) for stars with 2000 K $\leq T_{\rm eff} \leq$ 10,000 K, [Z/H] $= 0.0$, -0.5, and -2.0, and log $g = 4.5$ to simulate photometric colors in the *HST* bands. We found that using different metallicities changes the best-fit $T_{\rm eff}$ by 50–450 K for G0 and later type stars, and the spectral types obtained from metal-poor atmosphere models are usually 1–2 later in spectral type, e.g., M2 instead of M0, than the ones obtained from the models with solar metallicity. We also used Kurucz model atmospheres (Kurucz 1995) with 3500 K $\leq T_{\rm eff} \leq$ 6000 K to test the metallicity effect and found similar results. Using Girardi et al. (2002) theoretical isochrones, we estimate M_V and M_{F606W} for different metallicities for the point sources in our sample. Spectral types from the SED-fitting procedure (using the Pickles library), estimated absolute magnitudes, derived distances, and tangential velocities are given in Table 3. The ranges of absolute magnitudes, distances, and tangential velocities show the effect of using models with different metallicities. Despite these potential systematic errors, the total information we have available for the point sources (the morphological information, proper-motion measurements, and SED-fitting results) is sufficient to determine their nature.

6.1. *Late-Type Stars in the Galaxy*

Figure 9 shows the histogram of the number of stars observed at a given distance in the HDF-S, along with the predictions from the star count models (Reid & Majewski 1993; *dashed line*) and the observed distribution of stars in the HUDF (Pirzkal et al. 2005; *solid line*). The top panel shows the distribution of stars if we use the Pickles main-sequence library, and the bottom panel shows the same distribution if we use synthetic spectra with [Z/H] $= -2.0$ (halolike metallicity). Both panels show that there is a deficit of stars in the 5–15 kpc range in the HDF-S compared to the star count models.

If we assume that all of the stars in the HDF-S have solar metallicity, then we see an excess number of stars at $\sim$35 kpc

Object	Type	M_{F606W}	d (kpc)	$V_{\rm tan}$ (km s^{-1})
10663.........	K1–M0	5.73–8.25	1.5–4.8	84–269
10692.........	A3–A4	1.42–4.97	7.1–36.4	189–948
10017.........	K5–K6	7.33–10.58	0.9–3.9	...
10666.........	M2	9.17–11.09	0.8–1.9	36–87
10151.........	QSO	$z = 2.0$	...	...
10081.........	M5	12.18–12.46	0.9–1.0	118–134
1576...........	M3	10.19–12.56	0.7–2.2	75–222
2257...........	M3	10.19–12.56	1.2–3.4	...
10617.........	M5	12.18–12.46	1.7–1.9	188–214
86..............	G3	4.65–6.44	12.0–26.4	240–527
15..............	M3	10.19–12.56	1.4–4.2	...
2041...........	M5	12.18–12.46	2.2–2.5	67–76
10326.........	M2	9.17–11.09	2.3–5.5	216–522
701.............	M2.5	9.68–11.70	2.0–5.2	144–365
1922...........	M2	9.17–11.09	2.5–6.0	206–498
1209...........	M6	10.86–13.56	1.7–6.0	...
1257...........	M5	12.18–12.46	2.6–3.0	119–136
431.............	K1	5.73–7.24	15.1–30.3	200–400
1187...........	M1	8.69–11.14	3.4–10.5	...
2469...........	K1	5.73–7.21	15.9–31.5	442–874
323.............	K1–K3	5.73–7.43	15.7–34.4	434–949
108.............	M1	8.69–11.14	3.7–11.6	237–731
1444...........	B8–B9	-1.39–0.09	379.2–690.0	37875–68921
1444...........	WD	11.95	1.482	148 ± 56
2364...........	M5	12.18–12.46	3.7–4.2	48–54
1724...........	K3	6.58–7.68	15.2–25.3	324–537
1386...........	K6	7.59–10.64	4.4–18.0	231–942
933.............	M3	10.19–12.00	3.6–8.2	109–251
2072...........	M5	12.18–12.46	4.0–4.5	399–454
1331...........	M2	9.17–11.09	5.2–12.6	194–469
316.............	K7	7.86–11.15	4.8–22.0	121–552
1010...........	K3	6.58–7.41	23.1–33.9	...
1426...........	M0	8.25–11.13	6.1–22.8	388–1460
652.............	K6	7.59–10.50	7.9–30.1	236–901
191.............	M5	12.18–12.46	7.4–8.5	589–670
1302...........	M0	8.25–11.13	7.8–29.3	193–725
895.............	G0	4.18–5.98	93.5–208.4	15469–34471
895.............	WD	14.17	2.094	346 ± 79
2615...........	O9–M2	-4.32–11.09	14.6–17600	527–636472
1945...........	QSO	$z = 0.2$	...	...
2007...........	QSO	$z = 4.7$	...	...
2596...........	M0	8.25–11.13	14.2–53.3	127–479
441.............	M0	8.25–11.13	15.7–59.3	766–2886
1020...........	K7	7.86–11.15	15.6–71.1	713–3244
2178...........	QSO	$z = 4.0$	...	...
261.............	M0	8.25–11.13	22.2–83.5	623–2349
1306...........	M3	10.19–12.18	18.1–45.4	631–1577
2488...........	A0–A1	0.71–1.00	1350–1540	35803–40918
2488...........	WD	11.86	9.070	241 ± 303

and four more stars (HDFS 441, 1020, 2596, and 261) with estimated distances larger than 50 kpc, which is not expected from the star count models, nor would the distances be consistent with the metallicities for Galactic stars. Most of the objects observed at $\sim$35 kpc are K type stars, whereas the four objects with distances >50 kpc fit late-type star SEDs fairly well, and they have essentially the same spectral type (K7–M0). If we assume that their classification as point sources is reliable, our SED-fitting procedure works well to identify quasars and stars, and if we assume that they have solar metallicity, then we could claim that we discovered two new populations
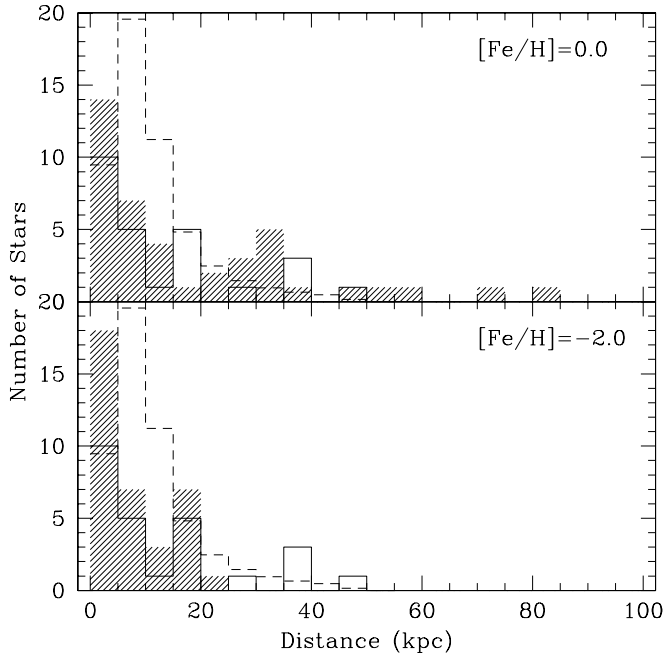
Fig. 9.—Histogram of the number of stars observed at a given distance in the HDF-S (*shaded histogram*) assuming solar (*top*) or metal-poor composition (*bottom*). The histogram of the number of stars observed in the HUDF (*solid line*) and the predictions from the star count models (*dash-dotted line*) are also shown.
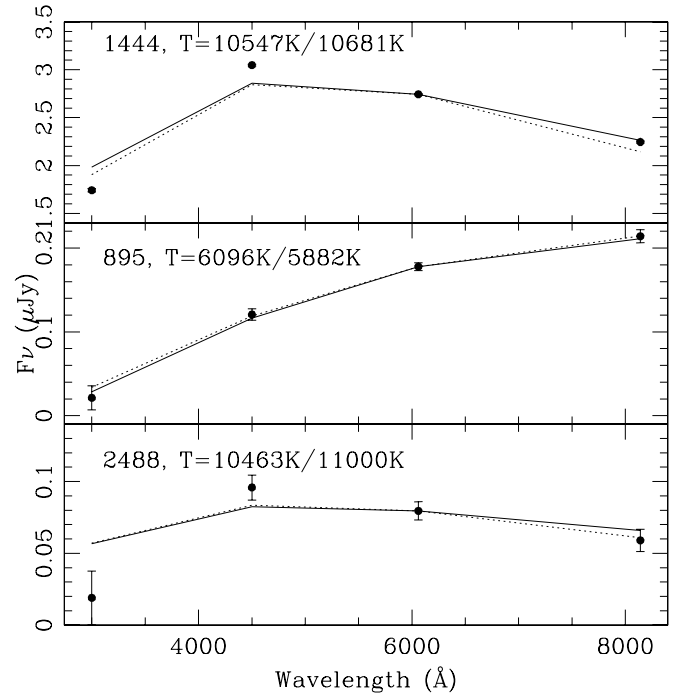

Fig. 10.—Fits to the spectral energy distributions of HDFS 1444, 895, and 2488. Best-fitting blackbody models are shown as solid lines, whereas best-fitting pure-H atmosphere white dwarf models are shown as dotted lines. The first temperature estimate in the label is for the blackbody, and the latter one is for the pure-H white dwarf models.

of stars, a cluster of stars at 35 kpc and several other stars at >50 kpc.

HDF-S and HUDF have similar Galactic latitudes ($-49°21$ and $-54°39$, respectively); therefore they should have similar distributions of Galactic objects. We do not find any stars with distances larger than 50 kpc in the HDF-N or the HUDF. Even though HDF-S ($l = 328°25$, $b = -49°21$) is about $25°$ away from the center of the Small Magellanic Cloud (SMC; $l = 302°80$, $b = -44°31$), the Magellanic Stream has overdense regions near the HDF-S (1×10^{19} atoms cm^{-2}; see the H I surface density maps of Mathewson & Ford [1984]). The average distance to the four objects with $d > 50$ kpc is 66.8 ± 13.4 kpc (assuming solar metallicity), whereas the distance to the SMC is measured to be 60.6 ± 3.8 kpc (Hilditch et al. 2005). Can these objects be members of the SMC? Assuming that they have metallicities similar to that of the SMC ([Fe/H] $= -0.7$; Lennon 1999), we estimate their average distance to be 17.8 ± 3.4 kpc; therefore they are not consistent with being in the SMC.

We expect the majority of the stars in the HDF-S to be halo stars (from the star count models and the velocity distribution of Fig. 7). Therefore, the bottom panel of Figure 9 is likely to represent the real distribution of stars better than the top panel. A comparison of the distances, tangential velocities, and photometric colors shows that all of the 42 stars except three (HDFS 1444, 895, and 2488) are consistent with being dwarf/subdwarf stars in the Galaxy. Seven of these 42 stars (HDFS 191, 1576, 1922, 2072, 10081, 10326, and 10617) show significant proper motion ($\mu/\sigma \geq 2$) and have spectral types M2–M5 and therefore are probable halo M dwarfs. Large errors in our proper-motion measurements prevent us from classifying the kinematic properties of the other stars; nevertheless, they are most likely to be G0 and later type dwarfs in the thick disk or halo of the Galaxy. The three stars (HDFS 1444, 895, and 2488) with estimated distances larger than 90 kpc (both for the metal-rich and for the metal-poor case) are discussed in § 6.2.

6.2. *White Dwarfs*

HDFS 1444, 895, and 2488 would have to be at very large distances (>90 kpc) if they were main-sequence stars of any metallicity. On the other hand, as white dwarfs, they would be at more reasonable distances. In order to find the temperatures of these objects, we simulated the colors for blackbody SEDs with temperatures in the range 3000–80,000 K. Figure 10 shows the best-fitting blackbody SEDs (*solid lines*) for HDFS 1444 (*top panel*), 895 (*middle panel*), and 2488 (*bottom panel*). We calculate the blackbody temperatures for these objects to be 10,547, 6096, and 10,463 K, respectively. We have also used DA white dwarf models (D. Saumon & D. Koester 2005, private communication) to simulate colors for white dwarfs with log $g = 8$ and 3000 K $\leq T_{\mathrm{eff}} \leq 20,000$ K. Cool white dwarfs show depressed infrared fluxes due to the effects of collision-induced absorption (CIA) due to molecular hydrogen (Hansen 1998; Saumon & Jacobson 1999). The pure-H white dwarf models that we used include the CIA opacities; therefore, we are able to compare the SEDs of young and old white dwarfs simultaneously and find the best-fit solution for our white dwarf candidates. Assuming that HDFS 1444, 895, and 2488 are pure-H atmosphere white dwarfs, we estimate the temperatures of these objects to be 10,681, 5882, and 11,000 K, respectively. Our best-fitting DA white dwarf SEDs are shown as dotted lines in Figure 10.

Using our best-fit DA white dwarf atmosphere solutions, we estimate the absolute magnitudes for our white dwarf candidates using the tables from Bergeron et al. (1995). We use the white dwarf models to predict M_{F606W} and therefore to calculate the distances and tangential velocities for these three objects. Estimated distances and kinematic properties of our white dwarf candidates are given in Table 3. HDFS 1444 displays a significant proper motion, 21.07 ± 7.93 mas yr^{-1} and is consistent with being a thick-disk or halo object at 1.5 kpc with
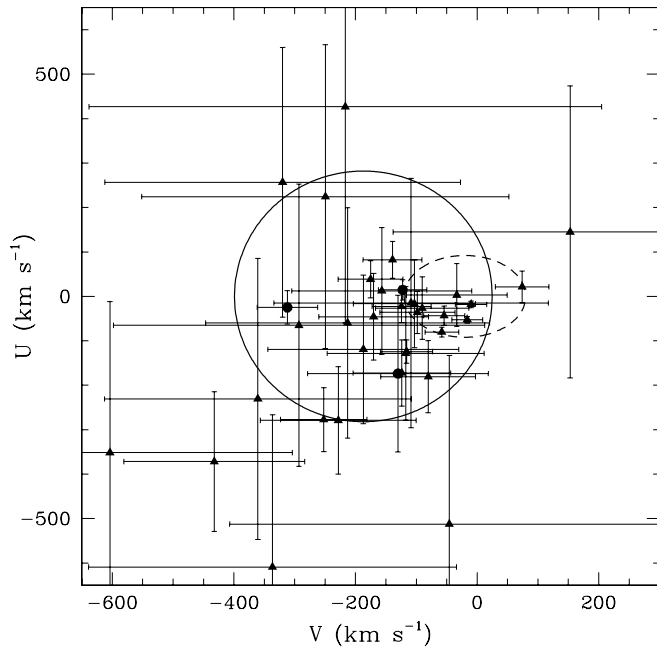
Fig. 11.—U vs. V diagram for the stars (*triangles*) and the likely white dwarfs (*circles*) in the HDF-S. The 2 σ velocity ellipse of the thick-disk objects is shown (*dashed line*), along with the 2 σ ellipse of the halo population (*solid line*). The errors in the tangential velocities are larger for distant objects; therefore these objects have also large error bars in the U vs. V diagram.

$V_{tan} = 148 \pm 56$ km s^{-1}. Likewise, HDFS 895 displays a proper motion of 34.9 ± 8.0 mas yr^{-1} and is more likely to be a halo white dwarf at 2.1 kpc with $V_{tan} = 346 \pm 79$ km s^{-1}. HDFS 2488 does not display any significant proper motion, and its classification as a point source is questionable (see § 2.1); nevertheless, if it is a star, then it would have to be a halo white dwarf at 9 kpc.

Figure 11 shows the U versus V velocity diagram for the stars (*triangles*; assuming $[M/H] = -2.0$) and the likely white dwarfs (*circles*) in the HDF-S. We use the results of Chiba & Beers (2000) for the expected velocity distribution of halo (*solid line*) and thick-disk (*dashed line*) objects. It is apparent from this figure that we have several thick-disk stars in our sample. Nevertheless, the majority of the stars are more likely to be in the Galactic halo. One of the white dwarf candidates, HDFS 1444, may well be a thick-disk white dwarf, whereas the other two candidates, HDFS 895 and 2488, are more likely to be halo white dwarfs.

6.3. *Mendez & Minniti Faint Blue Objects*

MM00 identified 10 faint blue objects in the HDF-S. We classified 2 of these 10 objects (HDFS 1812 and 1827) as resolved (see Fig. 2). We measure proper motions of 2.26 ± 7.93 and 3.25 ± 6.98 mas yr^{-1} for these two objects, respectively. One of the faint blue objects (HDFS 1332) is fainter than $I_{814} = 27$ (and therefore is not included in our analysis) and has a proper motion of 9.31 ± 7.93 mas yr^{-1}. Six of the faint blue objects (HDFS 1945, 2007, 2178, 441, 1020, and 261) have proper motions in the range 2.56–10.27 mas yr^{-1}. Our SED-fitting analysis showed that HDFS 1945, 2007, and 2178 have colors more consistent with being quasars than stars. In addition, we classify HDFS 441, 1020, and 261 as metal-poor stars in the halo of the Galaxy. Therefore, only one of the faint blue objects identified by MM00, HDFS 1444, plus two more white dwarf candidates

identified in our analysis (HDFS 895 and 2488), are consistent with being white dwarfs.

We use the Reid & Majewski (1993) star count models and our own calculations based on Gilmore et al. (1989; see Kilic et al. [2004] for a complete discussion) to predict the number of stars and white dwarfs expected in the HDF-S. We expect to find 45–52 stars and 0.66–2.31 white dwarfs, including 0.24–0.50 disk white dwarfs in the HDF-S. The star count models mildly overpredict the observed number of stars. The observed population of 2–3 white dwarfs is consistent with the standard Galactic models.

7. CONCLUSION

Superb resolution of the *HST* WFPC2 camera helped us to eliminate almost all of the large number of galaxies present in the HDF-S. Using accurate SED-fitting procedures (to eliminate quasars) and obtaining proper-motion measurements with a 3 yr baseline (to identify fast-moving halo objects) enabled us to classify the point sources in the HDF-S. We identified 4 quasars (consistent with zero proper motion) and 42 stars. Three of these stars (HDFS 1444, 895, and 2488), if they are on the main sequence, are too distant to be in the Galaxy and are best explained as white dwarf stars. Their kinematic properties show that HDFS 1444 is probably a thick-disk object, whereas the other two are more likely to be in the halo of the Galaxy. Third-epoch data on the HDF-S would be useful to place better constraints on the proper motions and the kinematic memberships of the point sources.

Figure 12 and 13 show the location of the stars, the quasars, and the white dwarf candidates in color-magnitude and color-color diagrams, respectively. A comparison of Figure 12 with Figure 3 of MM00 shows that a detailed analysis of the faint blue objects is needed to classify their nature; important additional constraints can be derived from SED fitting and from proper motions, even with a baseline of only 3 yr. The number
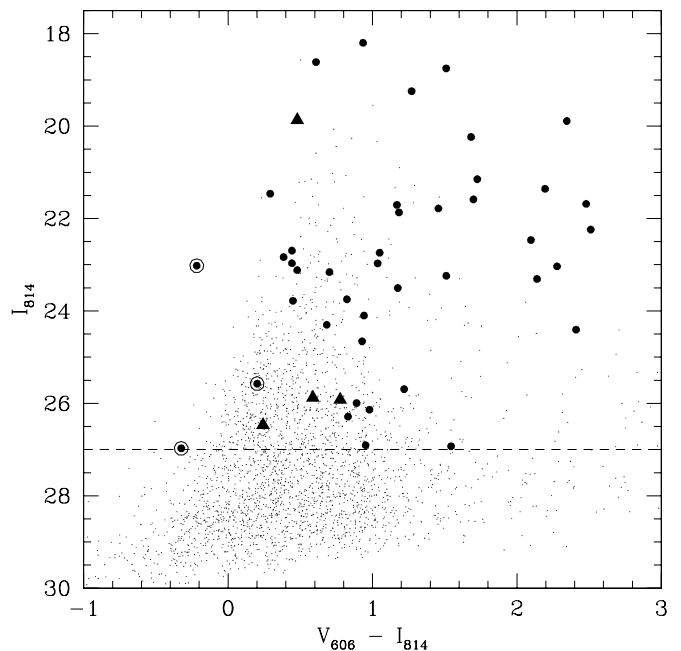

Fig. 12.—Location of the 46 point sources in a color-magnitude diagram. Filled circles and triangles represent stars and quasars identified from spectral energy distribution fitting, respectively. White dwarf candidates are also circled, whereas the smaller dots show the rest of the objects in the HDF-S catalog.
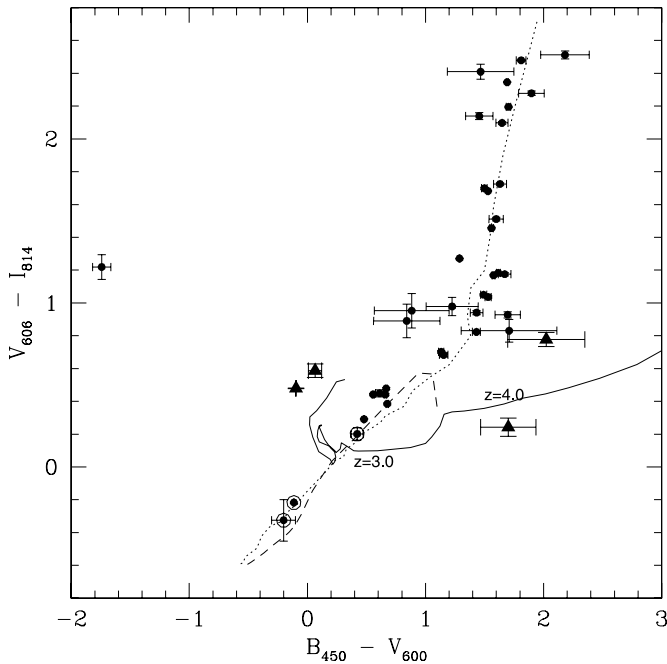
Fig. 13.—$V_{606} - I_{775}$ vs. $B_{435} - V_{606}$ color-color diagram for the stars (*filled circles*), the quasars (*triangles*) and the white dwarf candidates (*open circles*) in the HDF-S. Predicted tracks for main-sequence stars (O5–M6; *dotted line*), pure-H white dwarfs (log $g = 8$, $T_{\rm eff} = 60,000$–3000 K; *dashed line*), and quasars (*solid line*) are also shown.

of blue extragalactic sources is enormous at these magnitudes compared to the number of stellar objects. Our analysis shows that only two of the faint blue objects (HDFS 1444 and 895) show significant proper motion and are consistent with being disk/halo white dwarfs. None of the other faint blue objects exhibit significant proper motion, and therefore they are highly unlikely to be halo white dwarfs. Even if we misclassified a few blue extragalactic objects as unresolved, this would only decrease the observed number of stars and white dwarfs in the HDF-S and therefore strengthen our conclusion that the majority of the faint blue objects are not halo white dwarfs. The observed population of $\sim$2 white dwarf candidates ($I < 27$) in the HDF-N (Kilic et al. 2004), HDF-S (this study), and HUDF (Kilic et al. 2005) implies that the faint blue objects, especially the nonobserved population of halo white dwarfs, are highly unlikely to solve the dark matter problem.

REFERENCES

Alcock, C., et al. 2000, ApJ, 542, 281
Beckwith, S. V. W., et al. 2003, BAAS, 202, 1705
Bedin, L. R., Piotto, G., King, I. R., & Anderson, J. 2003, AJ, 126, 247
Bergeron, P., Ruiz, M. T., Hamuy, M., Leggett, S. K., Currie, M. J., Lajoie, C. P., & Dufour, P. 2005, ApJ, 625, 838
Bergeron, P., Wesemael, F., & Beauchamp, A. 1995, PASP, 107, 1047
Bertin, E., & Arnouts, S. 1996, A&AS, 117, 393
Brott, I., & Hauschildt, P. H. 2005, in Proc. Gaia Symposium, ed. C. Turon, K. S. O'Flaherty, & M. A. C. Perryman (ESA SP-576; Noordwijk: ESA), 565
Casertano, S., et al. 2000, AJ, 120, 2747
Chiba, M., & Beers, T. C. 2000, AJ, 119, 2843
Gilmore, G., King, I. R., & van der Kruit, P. C. 1989, in Saas-Fee Advanced Course 19, ed. R. Buser & I. R. King (Mill Valley: University Science Books)
Girardi, L., et al. 2002, A&A, 391, 195
Hansen, B. M. S. 1998, Nature, 394, 860
Hansen, B. M. S., et al. 2004, ApJS, 155, 551
Hilditch, R. W., Howarth, I. D., & Harries, T. J. 2005, MNRAS, 357, 304
Hoyos, C., Guzman, R., Bershady, M. A., Koo, D. C., & Diaz, A. I. 2004, AJ, 128, 1541
Ibata, R., Irwin, M., Bienaymé, O., Scholz, R., & Guibert, J. 2000, ApJ, 532, L41
Ibata, R. A., Richer, H. B., Gilliland, R. L., & Scott, D. 1999, ApJ, 524, L95
Kalirai, J. S., et al. 2004, ApJ, 601, 277
Kilic, M., von Hippel, T., Mendez, R. A., & Winget, D. E. 2004, ApJ, 609, 766
Kilic, M., von Hippel, T., & Winget, D. E. 2005, ApJ, submitted

Koekemoer, A. M., et al. 2002, HST Dither Handbook, Version 2.0 (Baltimore: STScI)
Kurucz, R. L. 1995, ASP Conf. Ser. 81, Workshop on Laboratory and Astronomical High-Resolution Spectra, ed. A. J. Sauval, R. Blomme, & N. Grevesse (San Francisco: ASP), 583
Lennon, D. J. 1999, Rev. Mex. AA, 8, 21
Mathewson, D. S., & Ford, V. L. 1984, in IAU Symp. 108, Structure and Evoultion of the Magellanic Clouds, ed. S. van den Bergh & K. S. de Boer (Dordrecht: Reidel), 125
Mendez, R. A. 2002, A&A, 395, 779
Mendez, R. A., & Minniti, D. 2000, ApJ, 529, 911 (MM00)
Mihalas, D., & Binney, J. 1981, Galactic Astronomy: Structure and Kinematics (2nd ed.; San Francisco: Freeman)
Oppenheimer, B. R., Hambly, N. C., Digby, A. P., Hodgkin, S. T., & Saumon, D. 2001, Science, 292, 698
Pickles, A. J. 1998, PASP, 110, 863
Pirzkal, N., et al. 2005, ApJ, 622, 319
Reid, I. N. 2005, ARA&A, 43, 247
Reid, N., & Majewski, S. R. 1993, ApJ, 409, 635
Reid, I. N., Sahu, K. C., & Hawley, S. L. 2001, ApJ, 559, 942
Reyle, C., Robin, A. C., & Creze, M. 2001, A&A, 378, L53
Richer, H. B. 2003, in The Dark Universe: Matter, Energy, and Gravity (Baltimore: STScI), 24
Saumon, D., & Jacobson, S. B. 1999, ApJ, 511, L107
Vanden Berk, D. E., et al. 2001, AJ, 122, 549
Werk, J. K., Jangren, A., & Salzer, J. J. 2004, ApJ, 617, 1004
Williams, R. E., et al. 1996, AJ, 112, 1335